J. Fluid Mech. (2008), *vol.* 616, *pp.* 43–61. © 2008 Cambridge University Press
doi:10.1017/S0022112008003066 Printed in the United Kingdom

Dynamics of bubbles near a rigid surface subjected to a lithotripter shock wave. Part 1. Consequences of interference between incident and reflected waves

J. I. ILORETA, N. M. FUNG AND A. J. SZERI

Department of Mechanical Engineering, University of California at Berkeley,
Berkeley, CA 94720-1740, USA
Andrew.Szeri@berkeley.edu

(Received 5 September 2006 and in revised form 3 May 2008)

In this paper we consider the dynamics of bubbles near a kidney stone subjected to a lithotripter shock wave. We address the effect of kidney stone geometry and composition on the cavitation potential near the stone in a shock wave lithotripter. The analysis is based on the previously developed work metric in which the work done on a bubble by the lithotripter shock wave (LSW) is used to determine the maximum radius the bubble achieves. Results of the reflection of the LSW from cylindrical kidney stones with proximal surfaces of varying geometry show that the presence of the stone enhances bubble growth near the stone and decreases growth further away, owing to constructive and destructive interference, respectively. These effects hold true regardless of the shape and curvature of the face, and are strongest for stones with concave faces and higher reflection coefficients. A consequence of the analysis is an elucidation of the mechanism for enhanced cavitation activity and creation of deep craters on the proximal side of a kidney stone, as have been observed in recent experiments.

1. Introduction

Shock wave lithotripsy (SWL), a non-invasive procedure that uses high-energy lithotriptic shock waves (LSWs) to treat kidney stones, has been used in clinical settings for over two decades now (Chaussy *et al.* 1982). In a typical procedure, approximately 2000 LSWs, generated extracorporeally, are focused at the site of the stone in order to pulverize the stone into grains that are fine enough to pass through the urinary system. Although SWL is very successful, the exact mechanism for stone comminution is still being debated. This is because the form of the LSW – an initial shock followed by a long rarefaction tail – admits several modes of stone destruction. One path of destruction is through compression-induced fracture, spallation, and/or squeezing caused by the leading shock of the LSW (Xi & Zhong 2001; Eisenmenger 2001). Another avenue of comminution is through cavitation damage, caused by the strong collapse of bubbles created by the long rarefaction tail of the LSW. A more plausible route combines the two mechanisms. An example might be spallation to break the stone into small chunks followed by cavitation to erode the chunks into fine grains.

In order to assess the different compression-induced comminution mechanisms, efforts have been made to determine the wave dynamics within kidney stones subjected to LSWs and how the wave dynamics affect the resulting stress fields. Dahake & Gracewski (1997) used an elastodynamic formulation to study spherical and ellipsoidal kidney stones to determine the effect geometry plays on the waves within stones. Xi & Zhong (2001) used photoelastic and shadowgraph imaging techniques to determine the stress fields in plaster-of-Paris stone phantoms. They showed that the location of cracks initiated by spalling depends greatly on the size and geometry of the stone. Cleveland & Sapozhnikov (2005) used a linear elastic model to show that the constructive interference of stress waves leads to high peak tensile stresses in stones.

There have also been efforts to investigate cavitation-induced damage to kidney stones. This type of damage is very clear in the high-speed photographs of kidney stones *in vitro* (Sass *et al.* 1991; Pishchalnikov *et al.* 2003). The pictures show that internal fissures created by the LSW become fluid-filled and provide nucleation sites for cavitation bubbles. These bubbles coalesce and form clusters that, upon collapse, lead to pits on the proximal end, cracks on the lateral faces, and slight damage on the distal end of stones. Because cavitation can be very damaging, controlling it to increase stone comminution has been a primary focus of the field. For example, Sokolov, Bailey & Crum (2001) developed a dual-pulse lithotripter and Xi & Zhong (2000) used a piezoelectric annular array generator in conjunction with an electrohydraulic lithotripter to force cavitating bubbles into stronger collapses.

In this work, we are interested in the interplay between cavitation and wave dynamics. In particular, we are concerned with the effect stone geometry has on the wave dynamics in the fluid near a kidney stone, and the subsequent changes this induces on the cavitation field. Similar studies have been done, but none have considered the stone in both the wave and bubble dynamics of the cavitation process. Tanguay (2004) developed a model of shock-wave propagation in a bubbly liquid mixture to determine the energy released during bubble collapses. However, he neglected the stone in treating the bubble collapses. Zabolotskaya *et al.* (2004) modelled the growth, coalescence and collapse of bubble clusters near a kidney stone. However, they neglected the effect of the stone on the pressure field and used an LSW without the reflected wave as the forcing pressure. In the present work, reflections from the stone are included. We also treat non-spherical bubble growth and collapse near a stone with an LSW that contains both the incident and reflected waves. We note that Ohl (2002) accounted for the stone in his work on bubble nucleation, but did not consider the effect of alterations in stone geometry.

This work is presented in two parts. In Part 1, we determine the pressure field resulting from the reflection of an LSW from stones of various shapes and composition. Then the dynamics of spherical bubbles associated with the different pressure fields are compared to assess the effect stone geometry has on the cavitation field near a kidney stone. In Part 2 (Calvisi, Iloreta & Szeri 2008), we investigate the consequences for the energetics of non-spherical collapses near stones using the pressure field calculated in Part 1 as input.

In both parts, we focus on the regime in which bubble clouds are sparse and the bubbles behave as though isolated, because this is what has been observed in experiments *in vivo* by Bailey *et al.* (2005). Our methods do not account for changes in shock dynamics due to the presence of a bubble, as experiments *in vitro* by Pishchalnikov *et al.* (2006) show that an LSW in the free field is not attenuated by growing bubbles. The experiments also show that an LSW near a kidney stone is not attenuated if a slow pulse repetition frequency is used, and stone comminution

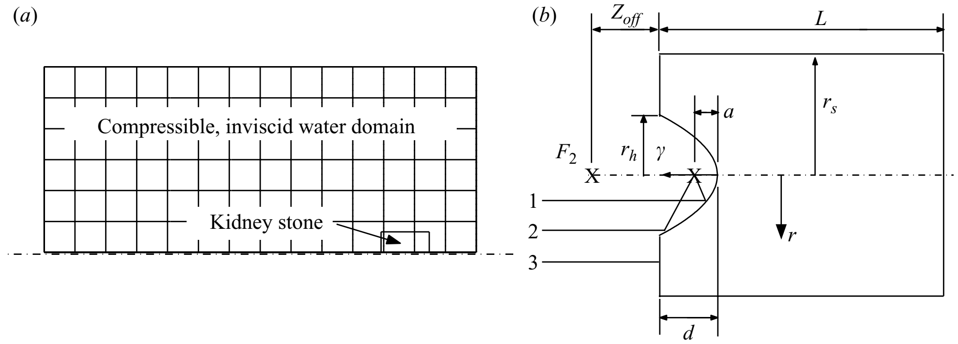

FIGURE 1. (*a*) A schematic of the cylindrical computational domain. The left, right and top boundaries are outflow boundaries, and the bottom is a reflective boundary as it serves as the axis of symmetry for the cylindrical domain. The shock wave (not shown) moves from left to right. Note that the computational grid is not drawn to scale. In (*b*) the kidney stone is enlarged and its dimensional parameters are outlined. Here, the bottom (revolved) half of the stone is also shown in order to avoid cluttering the dimensions. Note that this bottom half is not part of the computational domain (*a*).

is improved as a consequence. Note that our methods do account for the influence of the pressure wave on the bubble, and include the variations in the pressure field associated with incompressible liquid motions that accompany changes in bubble volume, and in Part 2, changes in bubble shape.

Part 1 is organized as follows. In § 2, we outline the methods we employ to determine the pressure field near a kidney stone. In § 3, we discuss the resulting pressure fields. In § 4, we determine the radial dynamics of spherical bubbles subjected to the pressure fields. In § 5, we present conclusions and concerns, and argue that new light has been shed on the mechanism for stone comminution.

2. Formulation

In this section, we present the numerical model for determining the pressure field around a kidney stone during SWL. In particular, the model calculates the dynamics of a shock wave that reflects from a cylindrical kidney stone and the pressure field that results from the interaction. Figure 1 shows the geometry of the problem. In figure 1(*a*), a shock wave (not shown) moves from left to right and is incident on a cylindrical kidney stone. An enlarged view of the stone is shown in figure 1(*b*).

The numerical model is based on an earlier scheme by Iloreta *et al.* (2007) developed to determine the flow field of a shock wave lithotripter. We outline the key points of the model for completeness. The flow field is governed by the axisymmetric Euler equations,

$$\frac{\partial}{\partial t}\boldsymbol{q} + \frac{\partial}{\partial r}\boldsymbol{F}(\boldsymbol{q}) + \frac{\partial}{\partial z}\boldsymbol{G}(\boldsymbol{q}) = \boldsymbol{S}(\boldsymbol{q}), \tag{2.1}$$

where the variables vector $\boldsymbol{q}$, the flux vectors $\boldsymbol{F}(\boldsymbol{q})$ and $\boldsymbol{G}(\boldsymbol{q})$, and the geometric source vector $\boldsymbol{S}(\boldsymbol{q})$ are defined as

$$\boldsymbol{q} = \begin{pmatrix} \rho \\ \rho u \\ \rho v \\ \rho e \end{pmatrix}, \quad \boldsymbol{F}(\boldsymbol{q}) = \begin{pmatrix} \rho u \\ \rho u^2 + p \\ \rho u v \\ (\rho e + p)u \end{pmatrix}, \tag{2.2a,b}$$

$$\boldsymbol{G}(\boldsymbol{q}) = \begin{pmatrix} \rho v \\ \rho u v \\ \rho v^2 + p \\ (\rho e + p) v \end{pmatrix}, \quad \boldsymbol{S}(\boldsymbol{q}) = \begin{pmatrix} -\dfrac{1}{r}\rho u \\ -\dfrac{1}{r}\rho u^2 \\ -\dfrac{1}{r}\rho u v \\ -\dfrac{1}{r}(\rho e + p) u \end{pmatrix}. \tag{2.2c,d}$$

Here $\rho(r, z, t)$ is the fluid density, $u(r, z, t)$ is the axial velocity, $v(r, z, t)$ is the radial velocity, $p(r, z, t)$ is the pressure, and $e(r, z, t)$ is the total mechanical energy per unit mass, defined as the sum of the kinetic energy per unit mass $|\boldsymbol{V}|^2/2 = (u^2 + v^2)/2$ and the strain energy per unit mass $\varepsilon = \int^{\rho} (p/\hat{\rho}^2)\,\mathrm{d}\hat{\rho}$.

The system of equations (2.1) is closed by specifying the Tait equation of state (EOS). With this EOS, the pressure in (2.2) is given by the Tait pressure

$$p \equiv p_{th} + B = \frac{B+1}{\rho_0^n}\rho^n, \tag{2.3}$$

and (2.2) has the same form as the equation of motion for an ideal gas ($p/\rho^{c_p/c_v} = \text{const}$). Thus, variables such as the sound speed are defined like those of an ideal gas. That is, the sound speed is given by $c = \sqrt{np/\rho}$ and the strain energy is given by $\varepsilon = p/(\rho(n-1))$. In the above, p_{th} is the thermodynamic pressure, c_p and c_v are the specific heats at constant pressure and volume, respectively, B (in units of atm) and n (unitless) are experimentally determined constants, and ρ_0 is the density at atmospheric pressure. The Tait EOS is valid for pressures up to 10^5 atm with $B = 3000$ atm and $n = 7$ (Batchelor 1967). Unless noted otherwise, hereinafter the Tait pressure will be implied when pressure is used.

The system of equations in (2.1) along with (2.3) is solved numerically using CLAWPACK (Conservation LAWs PACKage) (LeVeque 1997). CLAWPACK is a collection of Fortran subroutines that solves time-dependent hyperbolic systems based on a wave propagation algorithm. In this work we use the two-dimensional Euler package with a source term for the cylindrical geometry. The CLAWPACK algorithm is made second-order accurate with correction terms that use a monotonized-centred flux limiter. The correction waves are also propagated transversely in the wave propagation algorithm. The source term is handled using Godunov splitting, where a simple explicit Runge–Kutta method (the midpoint method) is used to solve the non-homogeneous equation. The computational domain in our work is a rectangular grid in the axisymmetric domain; for an example see figure 1(a). The left, top and right boundaries are ordinary outflow boundaries, while the bottom boundary is a reflective boundary because it serves as the axis of symmetry for the cylindrical domain.

2.1. *Kidney stone*

Rather than modelling the kidney stone as a rigid boundary (Tanguay 2004), in this work the kidney stone is approximated as an interface between two different regions within the computational domain (see figure 1a). The interface is defined by a surface such that grid cells lying inside the surface are in the stone domain while cells outside are in the fluid domain. Grid cells cut by the surface are given properties of both domains, weighted by the volume of each domain contained by the grid cell. To simplify the problem, we model the solid reflector domain as a liquid with the same EOS (but different properties) as the fluid domain. By doing so, the entire computational domain is governed by the same set of equations and eliminates the need to couple regions together where different equations (e.g. the Euler equations coupled with the linear elasticity equations) are solved. Moreover, it is a simple matter to consider stones of different shapes.

The reflection problem is treated by setting the initial properties of the stone domain such that the reflection coefficient across the water/pseudo-stone computational interface matches the actual reflection coefficient across the water/stone interface. In this study, we take the reflection coefficient as the ratio of pressure amplitudes as opposed to energy amplitudes:

$$R \equiv \frac{p^-}{p^+} = \frac{Z_2 \cos\theta_i - Z_1 \cos\theta_t}{Z_2 \cos\theta_i + Z_1 \cos\theta_t}\,. \tag{2.4}$$

Here p^- and p^+ are the amplitudes of the reflected and incident waves, respectively, $Z_j = \rho_j c_j$ is the impedance of the jth medium, θ_i is the angle of incidence, and θ_t is the angle of transmission. The sound speed $c_j = \sqrt{np_j/\rho_j}$, and the angles of incidence and transmission are related by Snell's law ($c_1 \sin\theta_t = c_2 \sin\theta_i$). Here, and throughout the rest of the paper, subscript 1 refers to water and 2 to the kidney stone.

To determine the initial properties of the pseudo-stone in the computational domain, the actual reflection coefficient across the water/stone interface is first calculated by using experimentally measured data for density and sound speed in (2.4). Then, the properties of the pseudo-stone are calculated with an expansion of (2.4) using the relationships above:

$$R = \frac{\sqrt{(p_2/p_1)(\rho_2/\rho_1)}\cos\theta_i - \sqrt{1 - \dfrac{(p_2/p_1)\sin^2\theta_i}{(\rho_2/\rho_1)}}}{\sqrt{(p_2/p_1)(\rho_2/\rho_1)}\cos\theta_i + \sqrt{1 - \dfrac{(p_2/p_1)\sin^2\theta_i}{(\rho_2/\rho_1)}}}. \tag{2.5}$$

As (2.5) states, the reflection coefficient of the computational domain is only a function of the pressure ratio p_2/p_1, the density ratio ρ_2/ρ_1 and the angle of incidence θ_i. Thus, we are free to vary any or all of these parameters to change the reflection coefficient in our computational domain. In our scheme, we choose to vary only the density ratio because a pressure jump induces motion and the angle of incidence is fixed by the geometry of the stone. Thus, the pseudo-stone is simply modelled as a density jump across a prescribed boundary. The density ratio ρ_2/ρ_1 is calculated using (2.5) with $p_1 = p_2$ for a given interface (R) and geometry (θ_i).

In our tests, we are interested only in the reflection very near the front of the stone because photographs by Pishchalnikov *et al.* (2003) show that damage is much greater to the proximal surface than to the lateral and distal faces. Thus, we need ensure only that the density of the proximal surface gives an accurate reflection. The density of the stone is set as follows. The actual reflection coefficient is determined for the kidney stone of interest. Then, the angle of incidence for a plane wave hitting the front of the stone is calculated as a function of radius r (see figure 1*b*). For example, the angle of incidence is 33° for line 1 in figure 2, 54° for line 2, and 0° for line 3. This step ensures accurate reflection from the proximal surface; if it is neglected, different parts of the LSW will reflect from the stone with different reflection coefficients. Finally, for a given radius, ρ_2 is determined from (2.5) with the θ_i determined at that radius. Grid points at that radius are given the pseudo-density ρ_2. A plane wave is used for this analysis because the incident LSW is almost planar in the focal region.

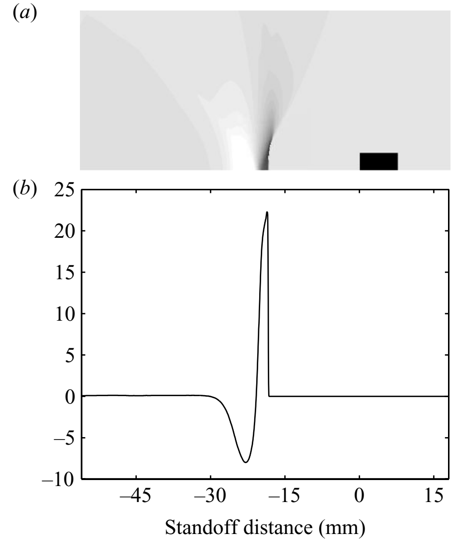

FIGURE 2. (*a*) The initial pressure field of the simulations. The initial pressure field is shown in a linear grey scale with the kidney stone domain in black. (*b*) The pressure along the symmetry axis. Note this wave is not yet fully developed, as it has not yet arrived at its focus.

Note that the reflection of the wave (within the kidney stone) from the distal side of the stone and subsequent re-transmission through the proximal side of the stone is not modelled because the transmitted wave has negligible amplitude by the time it re-enters the fluid. Although a naive analysis for the 'transmission/reflection/re-transmission' coefficient of a typical kidney stone shows that

$$TRT = \frac{4Z_1Z_2(Z_1 - Z_2)}{(Z_1 + Z_2)^3} \approx 0.4,$$

the experimental results of Pittomvils *et al.* (1996) show that the actual TRT is almost zero owing to the microscale heterogeneous internal structure of actual kidney stones (Zhodi & Szeri 2005). In other words, what is omitted in the simple foregoing analysis of TRT is the large attenuation of the wave with distance travelled in the stone.

Finally, bubbles on the surface of the stone created by an LSW and their effect on the reflection coefficient for the next LSW is not considered because the lifetime of cavitation bubbles is much shorter than the delay time between LSWs (Pishchalnikov *et al.* 2003, 2005). Also, bubbles on the surface of the stone created by an LSW do not affect the reflection coefficient for the same LSW because the bubbles are small during the residence time of the LSW; it is only when the LSW has long passed that the bubbles finally grow to an appreciable size.

2.2. *Initial conditions*

The simulations are initiated with a snapshot from an SWL model by Iloreta *et al.* (2007) of a Dornier HM3-like lithotripter. The model is the same as the one we based this analysis on; the parameters of the simulation are given in Iloreta *et al.* (2007). The initialization was implemented by taking the output of the flow variables, $\boldsymbol{q}$, from the full SWL model as input to the current simulations. Figure 2 shows the initial pressure field of the simulations. In the grey-scale plot, a flat-faced kidney stone is shown in black with the LSW located 15–20 mm in front of the stone (not yet fully developed). Note that we could have found the flow variables by another

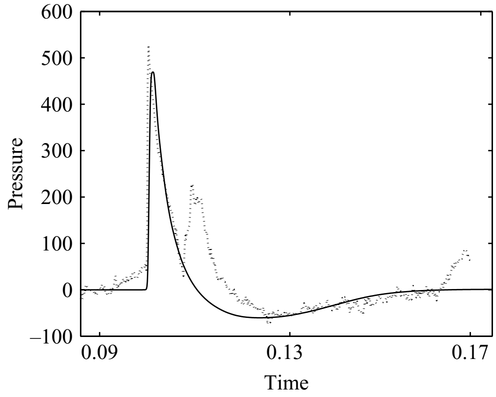

FIGURE 3. A typical pressure trace for a point on the symmetry axis for the no-stone test obtained by our simulation (solid) is compared with experimental data (dotted) measured by Zhou & Zhong (2003). The point chosen was the location of the proximal face of the kidney stone in § 3.2. The experimental data were obtained using a clinical HM-3 lithotripter (with cutouts for the imaging system) charged at 20 kV.

code or through experimental measurements (Averkiou & Cleveland 1999; Tanguay 2004; Zhou & Zhong 2006), but chose to take them from our code for convenience.

3. The pressure field near the proximal stone surface

In this section, we present the pressure fields due to the reflection of an LSW from various kidney stones and discuss the differences in these fields. In particular, we analyse the effects of kidney stone shape and composition on the pressure field near the proximal side of the stone. In all the tests, a cylindrical kidney stone was used. To test the effect of stone shape on the pressure field, the proximal surface of the stone was changed. Figure 1 (*b*) shows the parameters that govern the stone shapes used in the tests. Here, z_{off} is the (non-dimensional) distance the proximal face of the stone is from the second focus of the lithotripter (F_2) and γ is the (non-dimensional) standoff distance (as measured from the stone–liquid interface) along the symmetry axis.

Unless explicitly given, hereinafter all dimensions will be given in non-dimensional units. For consistency with Part 2 we choose the length scale to be the maximum radius a bubble located approximately 1 mm from the stone achieves when subjected to the tensile portion of the LSW in figure 2 ($R_m = 1168.83\,\mu\text{m}$), the pressure scale to be atmospheric pressure ($p_0 = 101\,325$ Pa), and the density scale to be the density of water at standard temperature and pressure ($\rho_0 = 998.0\ \text{kg}\,\text{m}^{-3}$). Consequently, the derived time scale is $R_m\sqrt{\rho_0/p_0} = 116.0\,\mu\text{s}$ and the derived energy scale is $p_0 R_m^3 = 161.8\,\mu\text{J}$.

3.1. *No stone*

To provide a basis for comparison, the simulation was first run without a stone. The simulation was run on a 1925 × 825 computational grid. The mesh size was $\text{d}x = 0.033$ and the time step was $\text{d}t = 8.62 \times 10^{-5}$. The maximum Courant number $\text{CFL}_{max} = 0.4065$ occurred at $t = 0.103$. The simulation was run for 4000 time steps and took 38 hours on a Pentium 4 PC. Figure 3 shows a typical pressure trace for a point on the symmetry axis obtained by our simulation (solid). The point chosen was the location of the proximal face of the kidney stone (see § 3.2). It is compared with experimental data (dotted) measured by Zhou & Zhong (2003) to illustrate that the properties of the pulse used in this study are relevant to SWL. The comparison

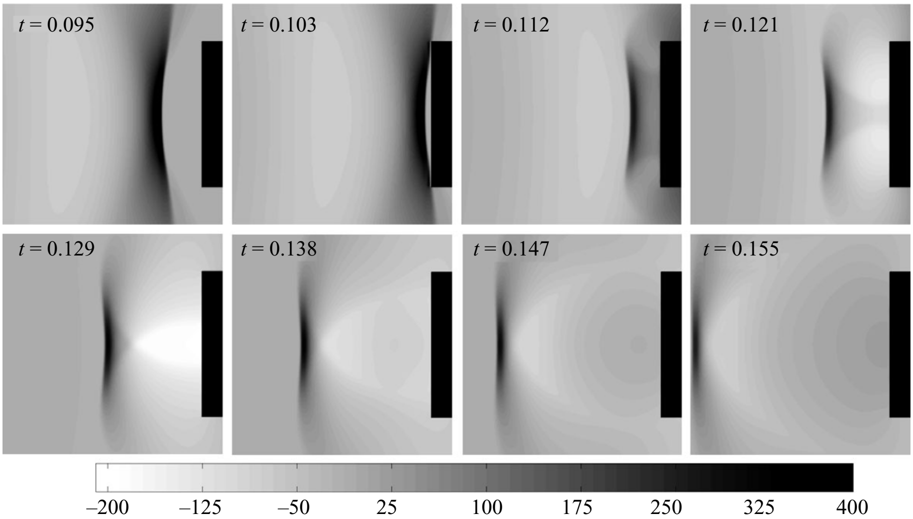

FIGURE 4. Snapshots of the pressure field at various times are shown in grey scale for reflection from a flat-faced cylindrical kidney stone. The real pressure in the kidney stone is not shown; rather it is given a value of 400 to aid visualization. The size of each frame is 8.56 × 8.56.

is excellent except that our simulation does not capture the secondary shock (second peak at $t = 0.114$) created by the cutouts for the imaging system in the experimental set-up; the cutouts were non-axisymmetric whereas the simulation was axisymmetric. Note that the peak of the pulse is almost double that of the initial pulse in figure 2 because the LSW focused as it propagated forward.

3.2. *Size of kidney stone*

Next we simulated a cylindrical stone with the following dimensions: length $L = 6.67$, radius $r_s = 2.82$, and z-offset $z_{off} = 12.49$. The stone had a flat front so the hole depth $d = 0$. A reflection coefficient of $R = 0.664$ was used because this corresponds to typical stone data from Pittomvils *et al.* (1995): $\rho_1 = 1000\ \mathrm{kg\,m^{-3}}$, $c_1 = 1500\ \mathrm{m\,s^{-1}}$, $\rho_2 = 1750\ \mathrm{kg\,m^{-3}}$, $c_2 = 4250\ \mathrm{m\,s^{-1}}$ and $\theta_i = 0$ (plugging these numbers into (2.4) yields $R = 0.664$). By (2.5), this corresponded to pseudo-stone properties of $\rho_2 = 24\,536\ \mathrm{kg\,m^{-3}}$ and $c_2 = 295\ \mathrm{m\,s^{-1}}$. The LSW was initially located at $\gamma = 15.74$ on the proximal side of the stone. The simulation was run on the same grid as that used for the no-stone case.

Figure 4 shows the pressure field near the proximal surface of the stone at various times. At $t = 0.095$–0.103, the LSW is propagating toward the stone, and at $t = 0.112$, the LSW has just reflected from the stone. At $t = 0.112$–0.121, we can see the formation of an edge wave, a circular wave centred at corners of the stone domain. The edge wave is a toroidal diffraction wave produced by the diffraction of the incident LSW around the rim of the stone. It is composed of a leading rarefaction followed by a trailing compression, which is opposite to that of the incident LSW. At $t = 0.129$–0.138, the edge wave has focused on the symmetry axis and its two inner surfaces have passed through one another. The focusing produced a region of intense tensile stresses around the axis of the stone (light region at $t = 0.129$). At $t = 0.147$–0.155, the reflected wave is long past the kidney stone and incident wave.

The edge wave is of great interest because it significantly enhances the rarefaction tail in the reflected wave. It is shown in § 4 that this changes the dynamics of bubbles profoundly. To disaggregate the effects of the edge wave more clearly, a test was

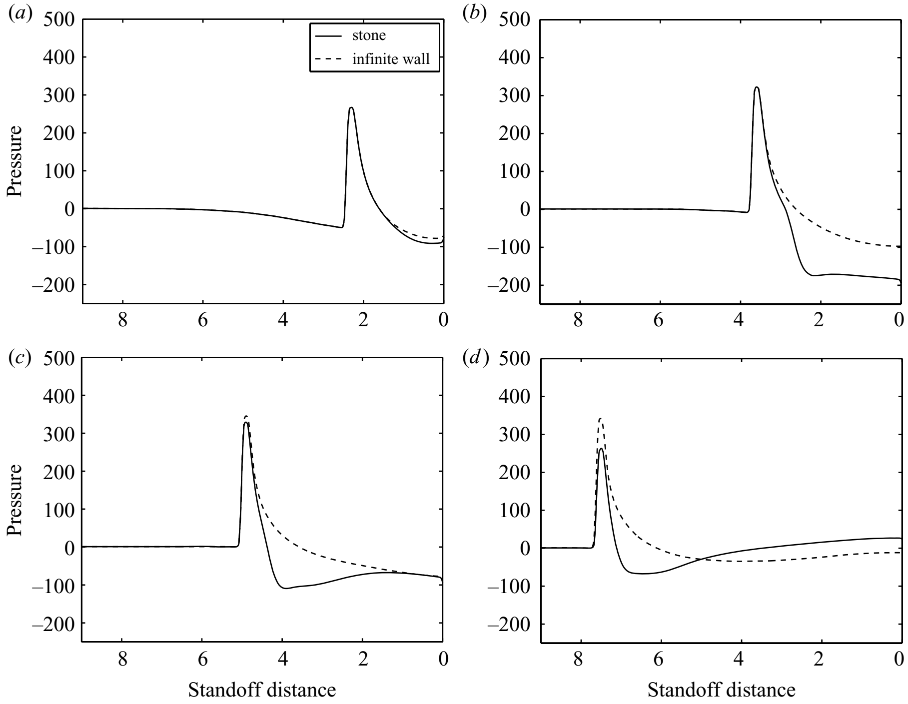

FIGURE 5. The pressures along the symmetry axis at various times are shown for reflection from a flat-faced, finite, cylindrical kidney stone and plane infinite wall: (*a*) $t = 0.121$, (*b*) $t = 0.129$, (*c*) $t = 0.138$, (*d*) $t = 0.155$.

done with a flat infinite wall to eliminate the edge wave. It was the same test as the foregoing, the only difference being that the stone radius was taken to be infinity; for the computation this corresponded to $r_s = 30$. The plots of pressure along the symmetry axis in figure 5 show the results of the test. The effect is most pronounced in figures 5(*b*) and 5(*c*). There it can be seen that the reflection from an infinite wall did not create an edge wave that focused on the symmetry axis. Thus the deepening of the rarefaction tail of the reflected wave did not happen. Without the edge wave, constructive and destructive interference between the incident and reflected waves were the only mechanisms that affected the pressure field. For the stone case, in figure 5(*a*), the shock of the reflected wave destructively interfered with the rarefaction of the incident wave, and in figures 5(*b*) and 5(*c*), the rarefaction of the reflected wave constructively interfered with the rarefaction of the incident wave. In figure 5(*d*), we see that the reflected wave had the same shape as the incident wave, but with a lower amplitude because part of the energy was transmitted into the kidney stone. Furthermore, the trailing compression of the edge wave has the additional effect of reducing the duration of the reflected rarefaction via destructive interference.

3.3. *Curvature of kidney stone*

Next we simulated a cylindrical stone with a curved proximal face to show the effects of stone shape on the pressure field near the proximal surface of the stone. In the first set of tests, the face had a concave shape given by a paraboloid. A paraboloid was chosen because it has a focus. The stone had the following dimensions: length $L = 6.67$, stone radius $r_s = 2.82$, hole radius $r_h = r_s$, hole depth $d = 0.428$, and z-offset $z_{off} = 12.49$. The focus of the paraboloid was at a distance $a = 4.71$. Again, a reflection

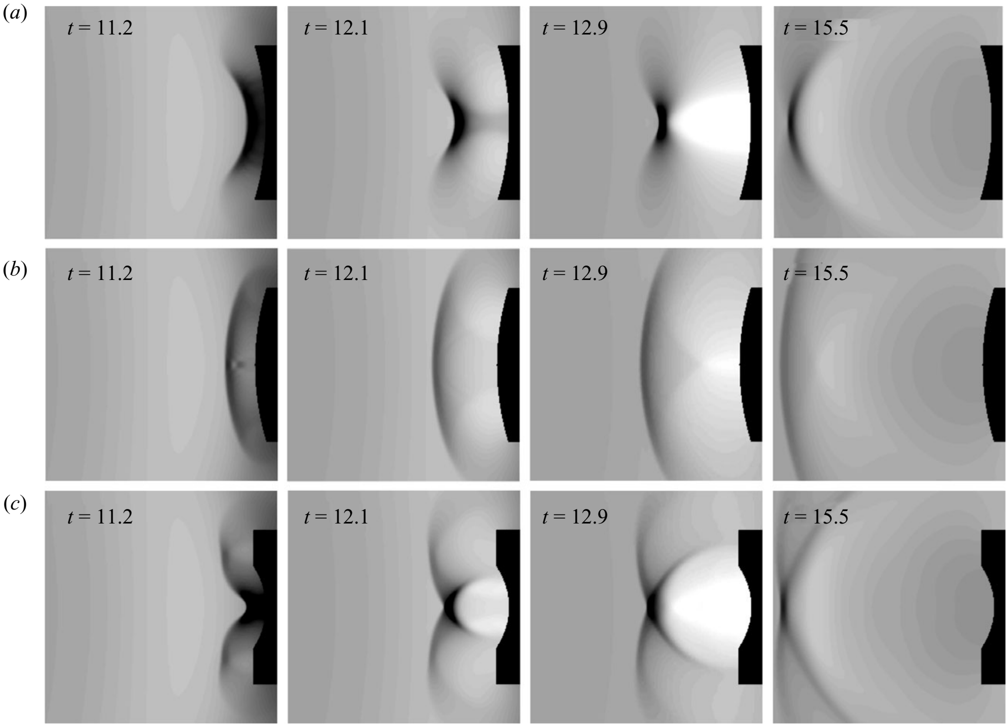

FIGURE 6. Snapshots of the pressure field at various times are shown in grey scale for reflection from a kidney stone with (*a*) a concave full-hole, (*b*) convex full-hole, and (*c*) concave half-hole. The pressure in the kidney stone is not shown. The same grey scale and frame size as in figure 4 is used.

coefficient of $R = 0.664$ was used and the LSW was initially located at $\gamma = 15.74$ on the proximal side of the stone. The simulation was run on the same grid as used for the no-stone case.

Figure 6(*a*) shows the pressure field near the proximal surface of the stone at various times. The focusing of the LSW is easily seen. At $t = 0.112$ the LSW has just reflected off the stone, at $t = 0.121$ the LSW has started to focus, and at $t = 0.129$ the LSW is focused. As in the cases for the flat stones, an edge wave produced by the rim of the kidney stone focused on the symmetry axis. We note that Sturtevant & Kulkarny (1976) studied a similar system of weak shocks in air and found similar results. However, the shocks in their study were canonical shocks in a sense that they were thin abrupt disturbances. In contrast, the shocks of the present study, composed of a shock and rarefaction, have an important spatial structure in the direction of propagation. This complicates the dynamics near the focal region. Unlike the system studied by Sturtevant & Kulkarny, here our pressure fields are determined from the interactions of both the compressions and rarefactions of the incident, reflected and edge waves. Sturtevant & Kulkarny give a detailed description of the focusing of a shock wave with a parabolic reflector.

To show the effect of stone curvature more clearly, a test was done using a convex paraboloid. The parameters of the stone were the same as the concave paraboloid case, the only difference being that the paraboloid was oriented in the opposite direction. Figure 6(*b*) shows the result of this test. It is easily seen that the reflected

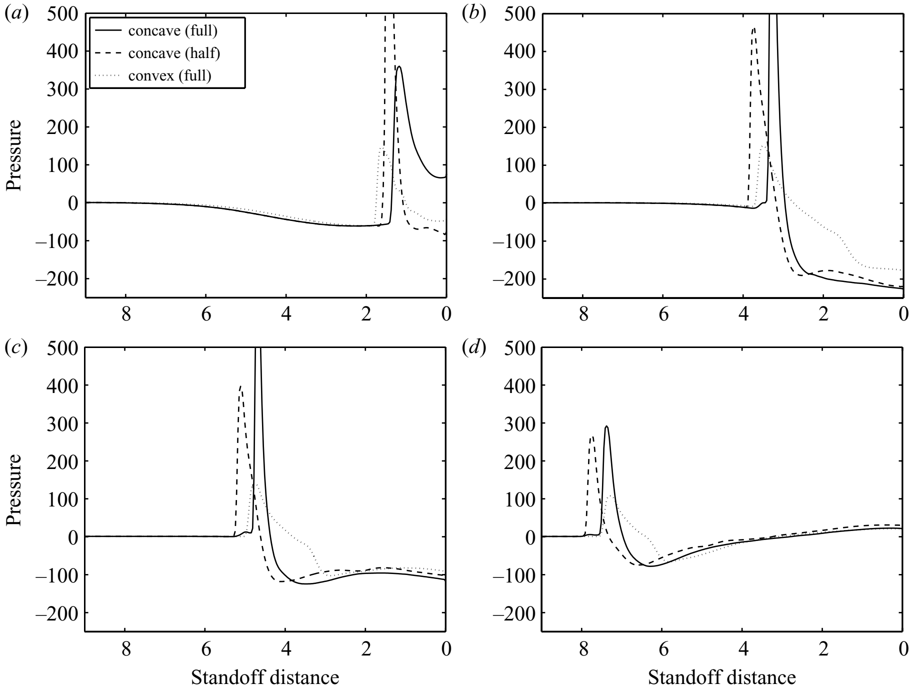

FIGURE 7. The pressures along the symmetry axis at various times are shown for reflection from a cylindrical kidney stone with a curved proximal face: (*a*) $t=0.116$, (*b*) $t=0.129$, (*c*) $t=0.138$, (*d*) $t=0.155$.

wave did not focus; instead, it diverged. Furthermore, the edge wave did not focus as strongly on the symmetry axis because it diverged as well. Another test was done to determine how the size of the 'hole' in the proximal face affects the pressure field. The test was similar to the concave paraboloid case, but only the centre of the kidney stone was given curvature; for the computation, the hole radius was $r_h=r_s/2$. Figure 6(*c*) shows the pressure field near the stone. There, the complicated dynamics of the multiple reflected and edge waves can be seen.

A more quantitative comparison of the three tests is shown in figure 7. There, the pressure along the symmetry axis at various times for the three cases is shown. At $t=0.116$, the half-hole case focused. Note that the peak of the pressure wave for the half-hole case ($p_{peak}=1362$) is not shown for better visualization of the differences between cases. At $t=0.129$, the full-hole case focused. However, the peak of the pressure wave for the full-hole case (again not shown for better visualization) was about half that of the half-hole case owing to tighter focusing in the latter. The focusing of the edge wave(s) for all the tests are also seen in this frame. In both concave tests, the peak negative pressure is about $p_{pn}=207$. In the convex test, the peak negative pressure is about $p_{pn}=173$. This is milder than the concave tests because of the divergence of the edge wave. At $t=0.155$, the divergence of the reflected wave for the convex case is seen as a reduction in pressure amplitude when compared to the concave cases. Lastly, the duration of the reflected compression is larger for the convex case than the concave cases because the edge wave arrives at the symmetry axis a little later owing to the increased distance it has to travel. Thus, the interference of the edge wave with the reflected compression is reduced.

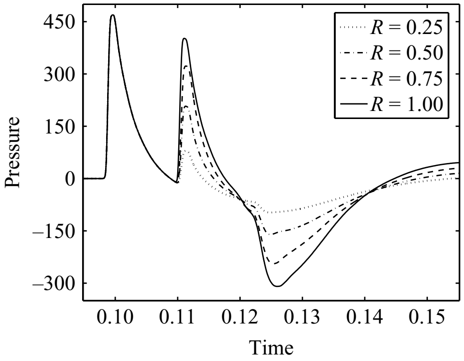

FIGURE 8. The pressure at a standoff distance of 0.86 is shown for flat-faced stones of varying composition.

3.4. *Composition of kidney stone*

Finally, we simulated cylindrical kidney stones of varying composition by changing the reflection coefficient of the stone. The stones had the same dimensions as the stones in § 3.2 and the simulations were run on the same grid as those stones as well. Figure 8 shows the pressure at a standoff distance $\gamma = 0.86$ for various stones. The range $0.25 \leqslant R \leqslant 0.75$ was chosen because measurements by Heimbach *et al.* (2000) of real and artificial kidney stones showed that the reflection coefficients lie within this range. The first peak in figure 8 is the incident shock and the second peak is the reflected shock. The effect of composition is seen through the amplitude of the reflected wave.

The most important result of this test is that the rarefaction tail of the reflected wave is greatly affected by the composition of the stone. This is because the stone composition affects the strength of the reflected wave and, consequently, the constructive interference of the rarefaction tails of the incident and reflected waves. For very reflective stones, the interference is high, whereas for slightly reflective stones, the interference is low. Also, diffraction of the incident wave is greatly affected by the composition of the stone. For very reflective stones, diffraction is high, whereas for slightly reflective stones, diffraction is low. In § 4, we show that these effects play a huge role in the bubble dynamics near kidney stones.

4. Bubble dynamics near the proximal surface of a stone

In this section, we quantify the differences in the pressure fields of § 3 following the analysis of Iloreta *et al.* (2007). In their analysis, the authors found that the work done on a bubble by the LSW correlates well with the maximum radius achieved by the bubble and argued that maximum radius is the key parameter for characterizing SWL because it is a good indicator of the damage bubbles could potentially cause (to the stone and tissue) during the procedure.

To calculate the work done on a bubble from r_1 to r_2 (t_1 to t_2),

$$W = \int_{r_1}^{r_2} (force)\,\mathrm{d}r = \int_{t_1}^{t_2} (-P \times area)\dot{r}\,\mathrm{d}t = -4\pi \int_{t_1}^{t_2} P r^2 \dot{r}\,\mathrm{d}t\,, \tag{4.1}$$

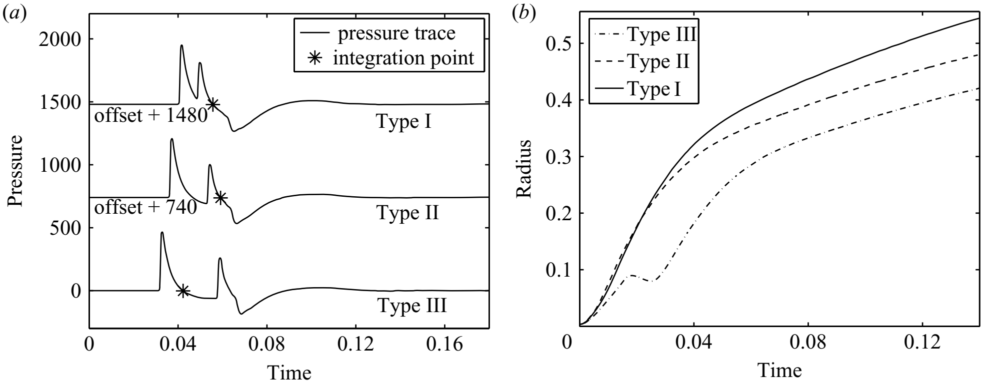

FIGURE 9. Typical pressure waves (*a*) and the corresponding bubble dynamics (*b*) are shown. In (*a*), the starting points for the integration of (4.2) are marked with a star.

we must first determine the radial bubble dynamics, $r(t)$, associated with the various external pressure fields $P(t)$. This is done using the Rayleigh equation

$$\rho_l\left(r\ddot{r} + \tfrac{3}{2}\dot{r}^2\right) = -P(t), \tag{4.2}$$

where ρ_l is the liquid density. Here, a dot represents a time derivative, so $\dot{r}(t)$ is the bubble wall velocity and $\ddot{r}(t)$ is the acceleration. Equation (4.2) is used instead of a full Rayleigh–Plesset (RP) equation because Hilgenfeldt *et al.* (1998) found that only these terms contribute significantly during the expansion phase of bubble growth. It is only this phase that is of interest because the shock wave passes long before the bubble reaches maximum volume. Thus, there is no contribution to (4.1) after the initial expansion because $P(t) = 0$. Also, the Rayleigh equation is used instead of the Gilmore equation because compressible effects are small in the bubble regime we are interested in. During bubble expansion, the bubble wall Mach number is at most $\dot{r}/c \sim 150\ \mathrm{m\,s^{-1}}/1500\ \mathrm{m\,s^{-1}} = 0.1$.

With the work known, the maximum radius is calculated with the following fit from Iloreta *et al.* (2007)

$$r_{max} = 0.6238\, W^{0.337}, \tag{4.3}$$

where r_{max} and W have been made dimensionless using the length and energy scales derived in § 3, respectively. The fit was made using a full RP equation that accounted for gas diffusion, heat transfer, chemical reactions, surface tension and viscous effects. We note that (4.3) can be interpreted as work being proportional to volume.

Equation (4.2) was solved for the various pressure fields using a Runge–Kutta solver in Matlab. In all the tests, the initial radius of the bubble was $r_0 = 0.00385$ (4.5 μm) and the initial wall velocity was $\dot{r}_0 = 0$. The initial radius was not varied because Church (1989) found that bubbles of initial radii in the range 1–10 μm achieve essentially the same maximum radius if driven by LSWs with peak positive pressures greater than 25 MPa. Furthermore, in Part 2, we show that this result also holds for non-spherical bubbles. Typical pressure waves from our simulations are shown in figure 9(*a*). Depending on the standoff distance, the waveforms had either one or two rarefactions after the leading shock: type I waves had one rarefaction while types II and III waves had two rarefactions. Here, waves of increasing type correspond to waves of increasing standoff distance.

In our tests, we started the integration at the beginning of the first rarefaction in cases of type I because Church (1989) and Iloreta *et al.* (2007) have shown that the maximum bubble size achieved in such flows depends little on the initial conditions. Clearly, a spherical model is not appropriate in handling the details of the interaction with the leading shock; it was shown by Ohl & Ikink (2003) that bubbles can lose minute amounts of mass, and display jetting phenomena in such situations. However, there is plenty of time after the interaction with the leading compression wave and before significant growth in the subsequent rarefaction for surface tension and coalescence to restore the possibly fragmented bubbles before the onset of significant growth. Thus, the leading shock should not appreciably affect our maximum radii calculations and can be ignored for computational simplicity.

Likewise, in cases of type II the reflected compression is strong enough to drive a strong collapse in a bubble that has just begun to expand. By appeal to the slender dependence on initial conditions previously mentioned, in pressure waves of type II we assume for simplicity that bubbles are in a state similar to that of our generic initial conditions when we begin the calculation after the reflected compression. In support of this, we note the high-speed images by Sankin *et al.* (2005) show that bubbles re-expand (non-spherically) to a volume close to that of a spherical expansion and that the ratio between the diameters along the vertical and horizontal directions is nearly unity (~ 1.25). The assumption about type II waves comes into play only in a localized region away from the stone (see figure 10). In cases of type III, it was possible to integrate through the (less intense) interaction with the reflected compression wave. Figure 9(*b*) shows the dynamics of bubbles corresponding to the different pressure types.

The maximum radius fields of the various tests are shown in figure 10. Note that the jagged surfaces of the stone faces are due to the coarseness of the data we saved, and not due to the coarseness of the computational mesh. There are several things that stand out in the field plots. (i) The no-stone case is a medium grey throughout while the other cases have a dark region near the stone and a light region further removed. This showcases the main effect of the stone: it creates a region of high cavitation potential near its proximal surface regardless of its shape and curvature. The extent and intensity of the high-cavitation-potential region is, however, highly dependent on the geometry and composition of the proximal face of the stone. It is this issue that we are interested in most, and thus we focus on it in the subsequent paragraphs. (ii) There are thin white streaks that indicate the region of minimum cavitation potential caused by the destructive interference between the reflected shock and incident rarefaction. As we move away from the stone, the reflected shock moves through and past the incident rarefaction, thus reducing the work done on the bubble with increasing standoff distance. However, at distances greater than half of the LSW length (i.e. at distances > 4.3) there cannot be destructive interference. Thus, destructive interference is a concave function of standoff distance and the location of the white streak is the location of maximum interference (i.e. lowest cavitation potential). (iii) The concave stones exhibit regions of low cavitation potential around the symmetry axis away from the stone. This is due to the focusing of the reflected shock waves along the axis (Sturtevant & Kulkarny 1976), and consequently, the suppression of bubble growth there.

These effects, as well as the mechanisms discussed in § 3, are more clearly seen in the r_{max} *vs.* γ plots of figure 11. There, the maximum radii achieved along the symmetry axis for the different test cases are compared. Note that for small γ, the maximum radii were larger than the standoff distance. This is non-physical because

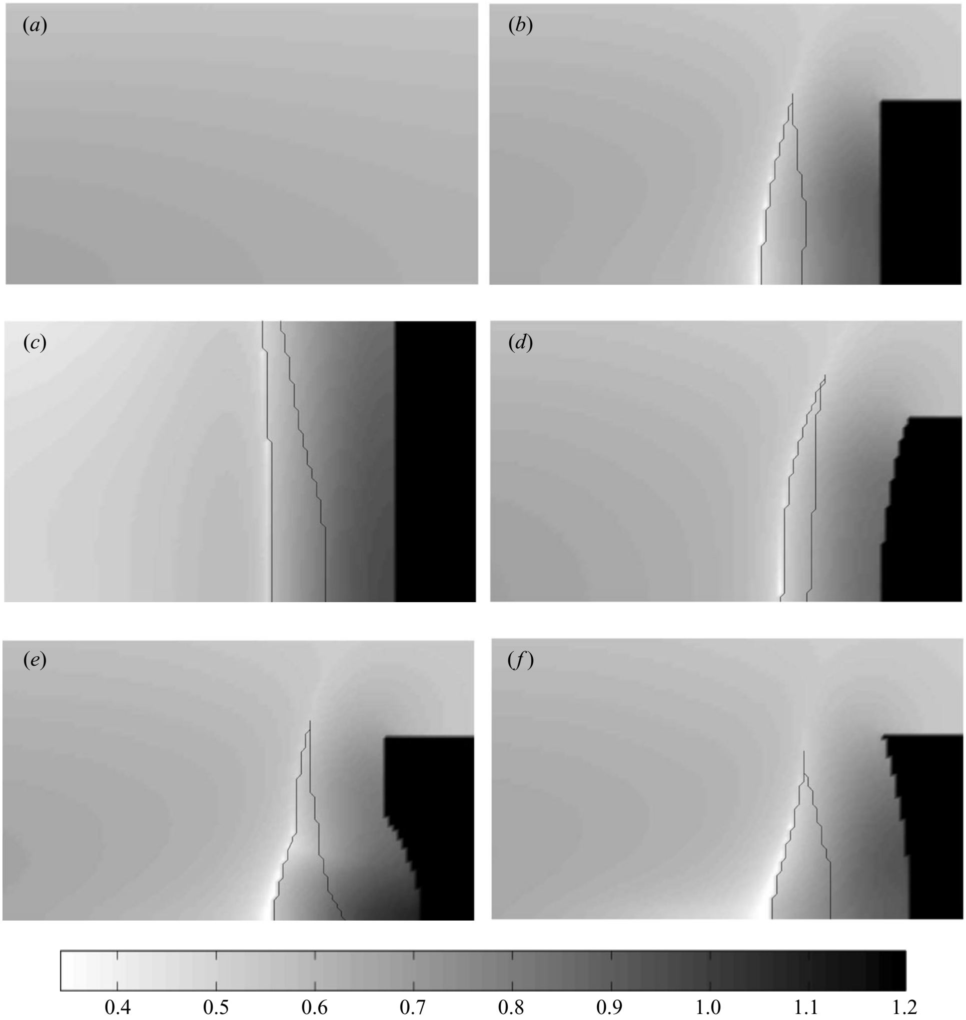

FIGURE 10. The maximum radius (mm) fields are shown for the various cases tested in § 3: (*a*) no stone, (*b*) flat stone, (*c*) infinite wall, (*d*) convex full-hole, (*e*) concave half-hole, and (*f*) concave full-hole. The radius fields in the kidney stones are given a value of 1.2 to aid visualization. Outlined by the light black lines are the localized regions in which bubble collapses due to the reflected compression wave are sufficiently strong that we expect the bubble fragments; hence we start the bubble dynamics following the reflected compression.

the stone makes the bubble grow asymmetrically at short distances and r_{max} may not be achieved. However, this analysis provides a first approximation to the changes of the bubble dynamics near a kidney stone in SWL. In Part 2, it is shown that the work correctly predicts the maximum volume – even for highly non-spherical bubbles.

In figure 11(*a*), the effect of the edge wave is seen through the differences in r_{max} for the infinite-wall case as compared with the flat-stone case. For the parameters tested, the maximum radii were higher by about 0.086 near the stone for the infinite wall and lower by about 0.128 away from the stone. This is counterintuitive because we would expect bubbles to grow larger near the stone for the flat-stone case because the edge wave deepens the rarefaction. However, this is not the case because of the structure of the edge wave: a tensile part followed by a compressive part. This

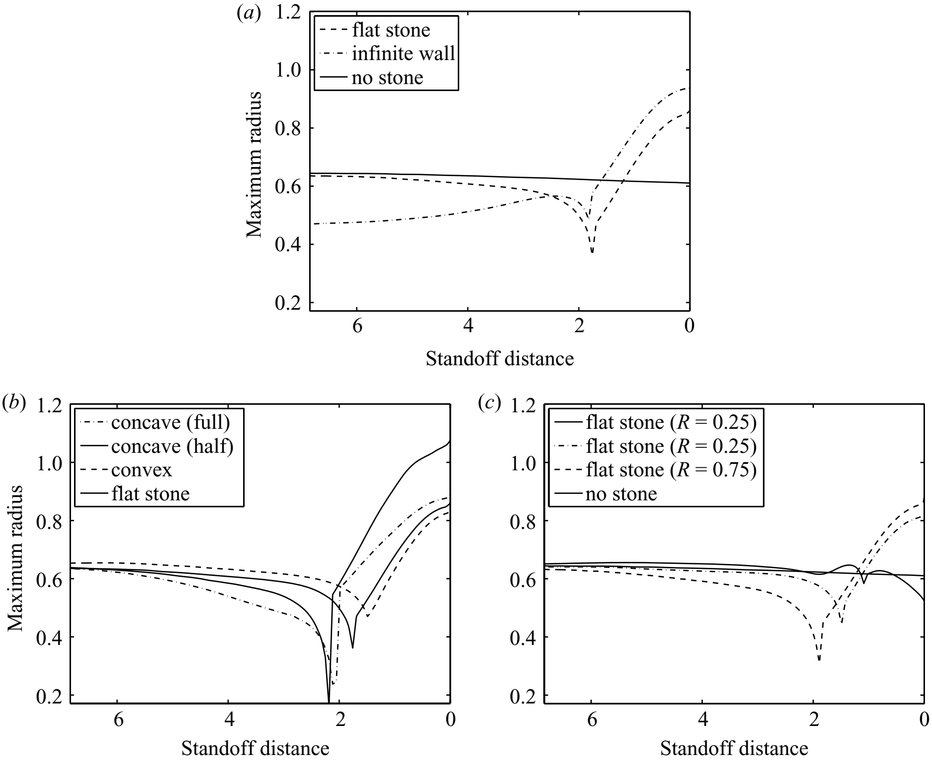

FIGURE 11. The maximum radii attained on the symmetry axis for the various cases tested in § 3 are compared.

structure, specifically the compressive part, creates a compression tail that follows the rarefaction of the reflected wave. Note that the rarefaction of the reflected wave is deepened by the tensile part of the edge wave. Figure 9(*a*) shows the compression tail as a slight rise in the pressure traces from $t = 0.08$ to 0.12 and figure 5(*d*) shows that the compression tail is not evident in the infinite-wall case. Now the apparent contradiction is eliminated: because the compression tail suppresses bubble growth and such a tail is not created in the infinite-wall case, bubbles grow larger near the stone for the infinite-wall case.

Away from the stone, the opposite is true because the edge wave focuses the reflected wave, and consequently, deepens the reflected rarefaction. Thus, the attenuation (owing to reflection from the stone) of the reflected wave for the flat-stone case is less than that for the infinite-wall case, and bubbles grow larger away from the stone for the flat-wall case. Also, figure 11(*a*) shows the effect of a kidney stone in the flow: it increases the size to which bubbles grow near the stone. For the no-stone case, $r_{max} \approx 0.6$. However, with a stone in the flow, $r_{max} \approx 0.86$. On a volume basis, this corresponds to a doubling of the maximum size to which bubbles grow.

In figure 11(*b*) this effect is even more pronounced owing to the focusing of waves. The strongest amplification occurred for the half-concave case in which bubbles grew to almost five times the size (by volume) of bubbles in a flow without a stone. Furthermore, the convex case also showed an increase in bubble radii near the stone, thus establishing that stones increase the cavitation potential of a shock wave lithotripter regardless of the shape of the stone. We also see the effect of shock focusing by the rapid reduction in r_{max} for the concave cases at about $\gamma = 2.14$.

In figure 11(c), the effect of stone composition is seen through the changes in the maximum radii due to the changes in the reflection coefficient. With increasing reflection coefficient, the cavitation potential increases near the stone and decreases further from it. This, too, is attributed to wave interference. Near the stone, an increase in constructive interference between the reflected and incident wave rarefactions increases the cavitation potential, and away from the stone, an increase in destructive interference between the reflected compression and incident rarefaction decreases the cavitation potential. The difference between a stone that has a reflection coefficient of 0.25 versus 0.75 may be greater than a factor of three.

We note that an interesting phenomenon in the region near the stone surface occurs at low reflection coefficient: bubbles grow larger without a stone present than when a stone with a low reflection coefficient is present. This is due to the compressive tail caused by the edge wave as described in figure 11(a). As the reflection coefficient is reduced, the strength of the reflected wave is reduced, and both the reflected rarefaction and compression tail are reduced proportionally. However, the reduction in the rarefaction affects bubble growth differently to the reduction in the compression tail because the compression tail acts on a larger surface area (i.e. when the bubble is larger). This nonlinearity explains why there should be regimes of reflection coefficients in which a change in the rarefaction dominates a change in the compression and regimes in which the effect is reversed. In this problem, at higher reflection coefficients, the change in the compression tail dominates.

Finally, the enhancement of bubble growth near the proximal surface of a stone helps explain an interesting mechanism for stone comminution. Suppose a flat (or even convex) stone is treated with SWL. A region of intense bubble growth will develop near the proximal surface. As shown in Part 2, these bubbles (or a larger bubble formed from the coalescence of smaller bubbles) will collapse asymmetrically and create jets that impact the stone. The result of the impact may be a small crater in the stone. If this happens, reflected waves from subsequent LSWs will focus along the symmetry axis of the crater and create even stronger bubble collapses which will tend to deepen the crater. The consequences of this can be seen in the experimental photographs by Pishchalnikov *et al.* (2003) of bubbles growing and collapsing on the proximal surface as well as the very deep crater that developed after the stone was treated with 50 LSWs.

5. Conclusions

In conclusion, we have shown how the presence of a kidney stone in the field of a shock wave lithotripter induces a reflection of the LSW that alters the pressure field near the stone. This alteration is caused primarily by the interference between the incident and reflected waves, and secondarily by edge waves that diffract from the stone. Near the proximal face of the stone, the rarefaction tends to be enhanced owing to constructive interference and edge-wave focusing. This effect is strongest for stones with concave faces and higher reflection coefficients. Further away from the stone, the rarefaction tends to be ameliorated owing to destructive interference between the reflected compression and the incident rarefaction.

A consequence of the changes to the pressure field induced by the presence of a stone is an alteration of the maximum size to which bubbles can grow. Near the stone surface, bubbles grow several times larger owing to the enhancement of the rarefaction, regardless of the shape and curvature of the proximal face. Further from the stone surface, bubbles grow several times smaller owing to destructive interference. The enhancement of bubble growth near the stone is two-fold for flat/convex faces and as high as five-fold for concave faces. Also, concave surfaces create a region of high cavitation potential at the focus of the surface.

Thus, we have shown that the stone and the reflection of the LSW from its surface play an important role in SWL and should be included in any analysis of the consequences of cavitation. In addition, experimentalists should be aware that artificial stones of different shapes and composition (reflection coefficient) alter the pressure field in different ways. This results in either a decrease or increase in the cavitation potential for bubbles near the stone, and consequently a decrease or increase in the vigour of cavitation and its role in stone comminution, respectively. Finally, the conclusions of this work may be applied to HIFU (high intensity focused ultrasound) in which bones may play a role similar to reflective kidney stones.

This work was funded by the the National Science Foundation Program in Biomedical Engineering. We would like to thank Dr Michael L. Calvisi for helping us with this problem and Ms Corinne Reich-Weiser for helping us with the figures.

REFERENCES

Averkiou, M. A. & Cleveland, R. O. 1999 Modeling of an electrophydraulic lithotripter with the KZK equation. *J. Acoust. Soc. Am.* **106**, 102–112.

Bailey, M. R., Pishchalnikov, Y. A., Sapozhnikov, O. A., Cleveland, R. O., McAteer, J. A., Miller, N. A., Pishchalnikova, I. V., Connors, B. A., Crum, L. A. & Evan, A. P. 2005 Cavitation detection during shock-wave lithotripsy. *Ultrasound Med. Biol.* **31**, 1245–1256.

Batchelor, G. K. 1967 *An Introduction to Fluid Dynamics*. Cambridge University Press.

Calvisi, M. L., Iloreta, J. I. & Szeri, A. J. 2008 Dynamics of bubbles near a rigid surface subjected to a lithotripter shock wave. Part 2. Reflected shock intensifies non-spherical cavitation collapse. *J. Fluid Mech.* **616**, 63–97.

Chaussy, C., Schmiedt, E., Brendel, W., Forssmann, B. & Walther, V. 1982 1st clinical-experience with extracorporeally induced destruction of kidney-stones by shock-waves. *J. Urol.* **127**, 417–420.

Church, C. C. 1989 A theoretical study of cavitation generated by an extracorporeal shock wave lithotripter. *J. Acoust. Soc. Am.* **86**, 215–227.

Cleveland, R. O. & Sapozhnikov, O. A. 2005 Modeling elastic wave propagation in kidney stones with application to shock wave lithotripsy. *J. Acoust. Soc. Am.* **118**, 2667–2676.

Dahake, G. & Gracewski, S. M. 1997 Finite difference predictions of p-sv wave propagation inside submerged solids. II. effect of geometry. *J. Acoust. Soc. Am.* **102**, 2138–2145.

Eisenmenger, W. 2001 The mechanisms of stone fragmentation in ESWL. *Ultrasound Med. Biol.* **27**, 683–693.

Heimbach, D., Munver, R., Zhong, P., Jacobs, J., Hesse, A., Müller, S. C. & Preminger, G. M. 2000 Analysis of Rayleigh–Plesset dynamics for sonoluminescing bubbles. *J. Urol.* **164**, 537–544.

Hilgenfeldt, S., Brenner, M. P., Grossman, S. & Lohse, D. 1998 Analysis of Rayleigh–Plesset dynamics for sonoluminescing bubbles. *J. Fluid Mech.* **365**, 171–204.

Iloreta, J. I., Szeri, A. J., Zhou, Y. F., Sankin, G. & Zhong, P. 2007 Assessment of shock wave lithotripters via cavitation potential. *Phys. Fluids* **19**, 086103.

LeVeque, R. J. 1997 Wave propagation algorithms for multidimensional hyperbolic systems. *J. Comput. Phys.* **131**, 327–353.

Ohl, C. D. 2002 Cavitation inception following shock wave passage. *Phys. Fluids* **14**, 3512–3521.

Ohl, C. D. & Ikink, R. 2003 Shock-wave-induced jetting of micron-sized bubbles. *Phys. Rev. Lett.* **90**, 214502.

Pishchalnikov, Y. A., Sapozhnikov, O. A., Bailey, M. R., Williams, J. C., Cleveland, R. O., Colonius, T., Crum, L. A., Evan, A. P. & McAteer, J. A. 2003 Cavitation bubble cluster activity in the breakage of kidney stones by lithotripter shockwaves. *J. Endourol.* **17**, 435–446.

Pishchalnikov, Y. A., Sapozhnikov, O. A., Bailey, M. R., Pishchalnikova, I. V., Williams, J. C. & McAteer, J. A. 2005 Cavitation selectively reduces the negative-pressure phase of lithotripter shock pulses. *Acoust. Res. Lett. Online* **6**, 280–286.

Pishchalnikov, Y. A., McAteer, J. A., Williams, J. C., Pishchalnikova, I. V. & Vonderhaar, R. J 2006 Why stones break better at slow shockwave rates than at fast rates: *in vitro* study with a research electrohydraulic lithotripter. *J. Endourol.* **20**, 537–541.

Pittomvils, G., Lafaut, J. P., Vandeursen, H., Boving, R., Baert, L. & Wever, M. 1995 Ultrasonic parameters of concentric laminated uric acid stones. *Ultrasonics* **33**, 463–467.

Pittomvils, G., Lafaut, J. P., Vandeursen, H., Boving, R., Baert, L. & Wever, M. 1996 Ultrasonic velocities of concentric laminated uric acid stones. *Ultrasonics* **34**, 571–574.

Sankin, G. N., Simmons, W. N., Zhu, S. L. & Zhong, P. 2005 Shock wave interaction with laser-generated single bubbles. *Phys. Rev. Lett.* **95**, 34501.

Sass, W., Bräunlich, M., Dreyer, H. P., Matura, E., Folberth, W., Priesmeyer, H. G. & Seifert, J. 1991 The mechanisms of stone disintegration by shock waves. *Ultrasound Med. Biol.* **17**, 239–243.

Sokolov, D. L., Bailey, M. R. & Crum, L. A. 2001 Use of a dual-pulse lithotripter to generate a localized and intensified cavitation field. *J. Acoust. Soc. Am.* **110**, 1685–1695.

Sturtevant, B. & Kulkarny, V. A. 1976 The focusing of weak shock waves. *J. Fluid Mech.* **73**, 651–671.

Tanguay, M. 2004 Computation of bubbly cavitating flow in shock wave lithotripsy. PhD thesis, California Institute of Technology.

Xi, X. F. & Zhong, P. 2000 Improvement of stone fragmentation during shock-wave lithotripsy using a combined EH/PEAA shock wave generator – *in vitro* experiments. *Ultrasound Med. Biol.* **26**, 457–467.

Xi, X. F. & Zhong, P. 2001 Dynamic photoelastic study of the transient stress field in solids during during shock wave lithotrispy. *J. Acoust. Soc. Am.* **109**, 1226–1239.

Zabolotskaya, E. A., Ilinskii, Y. A., Meegan, G. D. & Hamilton, M. F. 2004 Bubble interactions in clouds produced during shock wave lithotripsy. In *Proce. IEEE Ultrasonics Symp.* pp. 890–893.

Zhodi, T. I. & Szeri, A. J. 2005 Fatigue of kidney stones with heterogeneous microstructure subjected to shock-wave lithotripsy. *J. Biomed. Mater. Res.* B **75**, 351–358.

Zhou, Y. F. & Zhong, P. 2003 Suppression of large intraluminal bubble expansion in shock wave lithotripsy without compromising stone comminution: refinement of reflector geometry. *J. Acoust. Soc. Am.* **113**, 586–597.

Zhou, Y. F. & Zhong, P. 2006 The effect of reflector geometry on the acoustic field and bubble dynamics produced by an electrohydraulic shock wave lithotripter. *J. Acoust. Soc. Am.* **119**, 3625–3636.